

MEASUREMENT OF THE ABUNDANCE OF RADIOACTIVE ^{10}Be AND OTHER LIGHT ISOTOPES IN COSMIC RADIATION UP TO 2 GeV NUCLEON $^{-1}$ WITH THE BALLOON-BORNE INSTRUMENT ISOMAX

T. HAMS,^{1,2} L. M. BARBIER,³ M. BREMERICH,³ E. R. CHRISTIAN,¹ G. A. DE NOLFO,¹ S. GEIER,⁴
 H. GÖBEL,³ S. K. GUPTA,^{1,5} M. HOF,³ W. MENN,³ R. A. MEWALDT,⁴ J. W. MITCHELL,¹
 S. M. SCHINDLER,⁴ M. SIMON,³ AND R. E. STREITMATTER¹

Received 2004 March 9; accepted 2004 May 4

ABSTRACT

The Isotope Magnet Experiment (ISOMAX), a balloon-borne superconducting magnet spectrometer, was designed to measure the isotopic composition of the light isotopes ($3 \leq Z \leq 8$) of cosmic radiation up to 4 GeV nucleon $^{-1}$ with a mass resolution of better than 0.25 amu by using the velocity versus rigidity technique. To achieve this stringent mass resolution, ISOMAX was composed of three major detector systems: a magnetic rigidity spectrometer with a precision drift chamber tracker in conjunction with a three-layer time-of-flight system, and two silica-aerogel Cerenkov counters for velocity determination. A special emphasis of the ISOMAX program was the accurate measurement of radioactive ^{10}Be with respect to its stable neighbor isotope ^9Be , which provides important constraints on the age of cosmic rays in the Galaxy. ISOMAX had its first balloon flight on 1998 August 4–5 from Lynn Lake, Manitoba, Canada. Thirteen hours of data were recorded during this flight at a residual atmosphere of less than 5 g cm $^{-2}$. The isotopic ratio at the top of the atmosphere for $^{10}\text{Be}/^9\text{Be}$ was measured to be 0.195 ± 0.036 (statistical) ± 0.039 (systematic) between 0.26 and 1.03 GeV nucleon $^{-1}$ and 0.317 ± 0.109 (statistical) ± 0.042 (systematic) between 1.13 and 2.03 GeV nucleon $^{-1}$. This is the first measurement of its kind above 1 GeV nucleon $^{-1}$. ISOMAX results tend to be higher than predictions from current propagation models. In addition to the beryllium results, we report the isotopic ratios of neighboring lithium and boron in the energy range of the time-of-flight system (up to ~ 1 GeV nucleon $^{-1}$). The lithium and boron ratios agree well with existing data and model predictions at similar energies.

Subject headings: balloons — cosmic rays — nuclear reactions, nucleosynthesis, abundances

1. INTRODUCTION

It has long been understood that the relative abundances of the constituents of Galactic cosmic rays (GCRs) provide information about cosmic-ray transport within the Galaxy. In particular, cosmic rays of primary origin such as carbon, nitrogen, and oxygen may interact with the interstellar medium (ISM) to produce “secondary” fragments such as lithium, beryllium, and boron. The measured ratio of secondary to primary cosmic rays, e.g., boron/carbon, can be used to compute the mean amount of interstellar matter (i.e., path length) that cosmic rays have encountered before reaching the Earth, which ultimately provides important constraints on the composition and homogeneity of the ISM in which they propagate.

The simplest GCR transport model, the leaky-box model (LBM), assumes a Galaxy with uniform density from which cosmic rays escape or “leak” out with an energy-dependent probability per unit time. More realistic models, exemplified by those of Prishchep & Ptuskin (1975) and Ginzburg & Ptuskin (1976), account for the actual structure of the Galaxy, incorporating both a high-density central disk and a low-density halo. Recent models include the effects of cosmic-ray transport

within the Local Bubble (Ptuskin & Soutoul 1998; Moskalenko & Strong 2000; Streitmatter & Stephens 2001). There are a number of recent reviews Berezhinskii (1990), Stephens & Streitmatter (1998), Simon (1999), and Moskalenko (2003) of the cosmic-ray transport models and underlying computational techniques.

The cosmic-ray path length, determined from observations of stable secondary to primary nuclei, depends on both the average density traversed and the average lifetime of cosmic rays before escape from the Galaxy. On the other hand, unstable nuclei, such as ^{10}Be , ^{26}Al , ^{36}Cl , ^{54}Mn , and ^{14}C , act as radioactive “clocks,” providing additional constraints on the average lifetime of GCRs within the Galaxy and thus complementing the observations of stable GCR nuclei. Furthermore, extending observations of these clock isotopes to higher energies where the Lorentz factor significantly changes the decay lifetime offers a more sensitive test of cosmic-ray propagation. High-energy radioactive isotopes in the relativistic regime sample on average a larger region of interstellar space during propagation than low-energy GCRs. The secondary isotope ^{10}Be , which has a decay lifetime (1.6×10^6 yr) comparable to the average cosmic-ray confinement time within the Galaxy, is particularly well suited for cosmic-ray transport studies.

The Isotope Magnet Experiment (ISOMAX) was designed with the primary goal of measuring the radioactive isotope ^{10}Be beyond 1 GeV nucleon $^{-1}$ for the first time (Streitmatter et al. 1995). ISOMAX measures the composition of the light isotopes from lithium to oxygen using a balloon-borne magnetic rigidity spectrometer. In this paper, the results of the first

¹ Laboratory for High Energy Astrophysics, NASA Goddard Space Flight Center, Greenbelt, MD 20771; hams@milkyway.gsfc.nasa.gov.

² Resident Research Associate of the National Research Council.

³ Fachbereich Physik, Universität Siegen, 57068 Siegen, Germany.

⁴ Space Radiation Laboratory, California Institute of Technology, Pasadena, CA 91125.

⁵ HECR Group, Tata Institute of Fundamental Research, Mumbai 400 005, India.

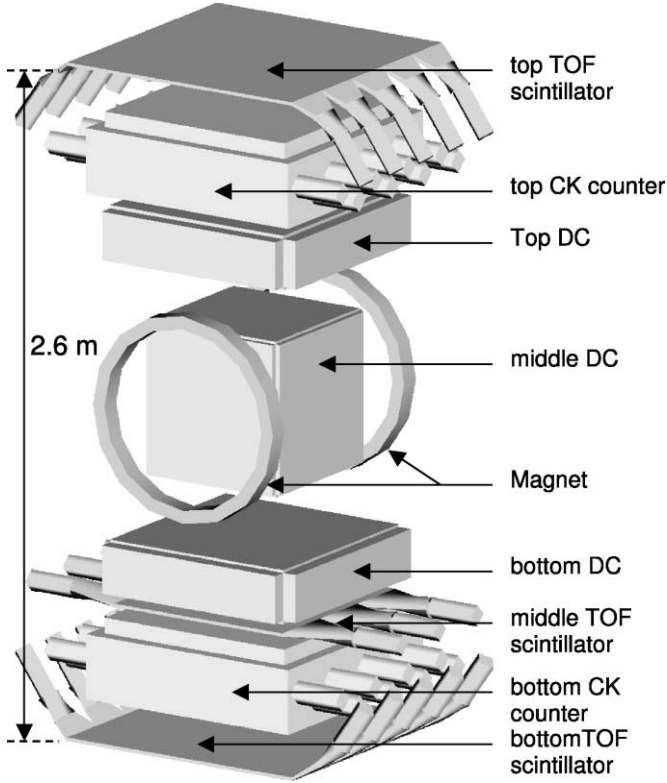


FIG. 1.—Schematic view of the ISOMAX instrument and its detector systems.

flight of ISOMAX on 1998 August 4–5 from Lynn Lake, Manitoba, Canada will be discussed and compared with previous measurements and model predictions.

2. ISOMAX INSTRUMENT

ISOMAX identifies incoming cosmic-ray particles by simultaneously measuring their charge, velocity, and magnetic rigidity (momentum per charge). The instrument was composed of three detector subsystems: a magnetic rigidity spectrometer using a drift chamber (DC) tracker, as well as velocity detectors consisting of a state-of-the-art time-of-flight (TOF) system, which also provided the charge determination, and two silica-aerogel Cerenkov (CK) counters. A schematic overview of the ISOMAX instrument is given in Figure 1. The particle rest mass m is determined by the velocity versus rigidity technique, given by the following equation:

$$m(\beta, Z, R) = RZe \frac{\sqrt{1 - \beta^2}}{\beta c}, \quad (1)$$

where R is the magnetic rigidity ($R \equiv p/Ze$) and Z and β are the particle charge and velocity. The complementary velocity detectors, i.e., TOF and CK, offer two independent methods to determine β . In the data analysis we refer to the TOF-rigidity or Cerenkov-rigidity technique, depending on which detector provided the velocity for the particle identification according to equation (1). The challenge of ISOMAX is to separate ^{10}Be from its neighboring isotope ^9Be , which requires excellent charge and mass resolution. A more detailed and general discussion of the instrument can be found elsewhere (Mitchell et al. 1999; J. W. Mitchell et al. 2004, in preparation; Hof et al. 2000).

2.1. Magnetic Rigidity Measurement

The magnetic rigidity R of incident particles is obtained from the track curvature in the presence of a known magnetic field. The rigidity is defined as $R = a|B| = p/Ze$, where a is the radius of the curvature of the particle track in the magnetic field B , and p and Z are the particle momentum and charge. The particle trajectory is measured by a stack of three high-resolution DCs. The middle DC is located in the high-field region between two Helmholtz-like coils of a superconducting magnet. The ISOMAX superconducting magnet had a split-pair design incorporating a large warm bore for the central DC tracking detector with a volume of $66 \text{ cm} \times 60 \text{ cm} \times 100 \text{ cm}$. Each of the two coils had an outer diameter of 78.8 cm and a cross section of $6.0 \text{ cm} \times 9.4 \text{ cm}$. The face-to-face separation of the coils was 80 cm. The coils were fabricated with a filament of NbTi in a copper matrix and held at the temperature of liquid helium. The cryogenic system in the magnet had a volume of 390 liters. The hold time of the charged magnet was 100 hr. A single service turret allowed for cryostat filling and coil charging. The service ports of the magnet were accessible outside of the instrument gondola, allowing the refill of the magnet shortly before launch. The ISOMAX magnet was built by the Special Project Group at Oxford Instruments, England. Further details on the magnet can be found elsewhere (Hams et al. 1999; Mitchell et al. 1999; J. W. Mitchell et al. 2004, in preparation). Prior to the flight the magnet demonstrated a persistent mode at a current of 160 A. For the flight we chose a conservative current of 120 A, resulting in a homogenous central field of 0.8 T between the coils and a magnetic field integral of $0.54 \text{ T} \times \text{m}$ within the tracking detector.

As shown in Figure 1, the tracking detector in the magnet spectrometer consisted of a stack of three high-resolution DCs with a total of 480 closely packed hexagonal drift cells. The cell radius was 1.35 cm. Pure CO_2 was used as a “slow” drift gas. The relatively low drift velocity in CO_2 minimizes the effects of the Lorentz force on the drifting electrons. The drift cells were arranged in 24 layers, of which 16 layers in the bending plane measured the curvature of the particle trajectory and the remaining eight layers were interleaved in the perpendicular nonbending plane. The electric field was maintained with high cylindrical symmetry within each cell for all relevant drift paths. To achieve good cylindrical symmetry, each drift cell consisted of a sense wire maintained at positive high voltage (HV) and surrounding grounded cathode and intermediate additional potential wires. The sense wires were composed of gold-plated tungsten with a diameter of $30 \mu\text{m}$, and the cathode and additional potential wires were composed of gold-plated tungsten with a diameter of $100 \mu\text{m}$. In addition, adjacent layers with orientations perpendicular to each other were separated by guard wires to minimize local field interference. For ground data ($Z = 1$ particles), the sense wires were held at a potential of 4.6 kV, while the additional potential wire was held at 1.14 kV. The guard wires were maintained at half the voltage of the additional potential wires. The maximum drift time for this setting was about $2.1 \mu\text{s}$. The field configuration of a drift cell with guard wires on top is shown in Figure 2.

The two outer chambers had a sensitive volume of $69 \text{ cm} \times 69 \text{ cm} \times 18.6 \text{ cm}$, and the middle DC, located in the high-field region in the warm bore of the magnet, had a sensitive volume of $47 \text{ cm} \times 47 \text{ cm} \times 58 \text{ cm}$. The overall height of the DC stack was 150 cm. The four walls of each chamber were composed of 1 cm thick aluminum-reinforced resin epoxy

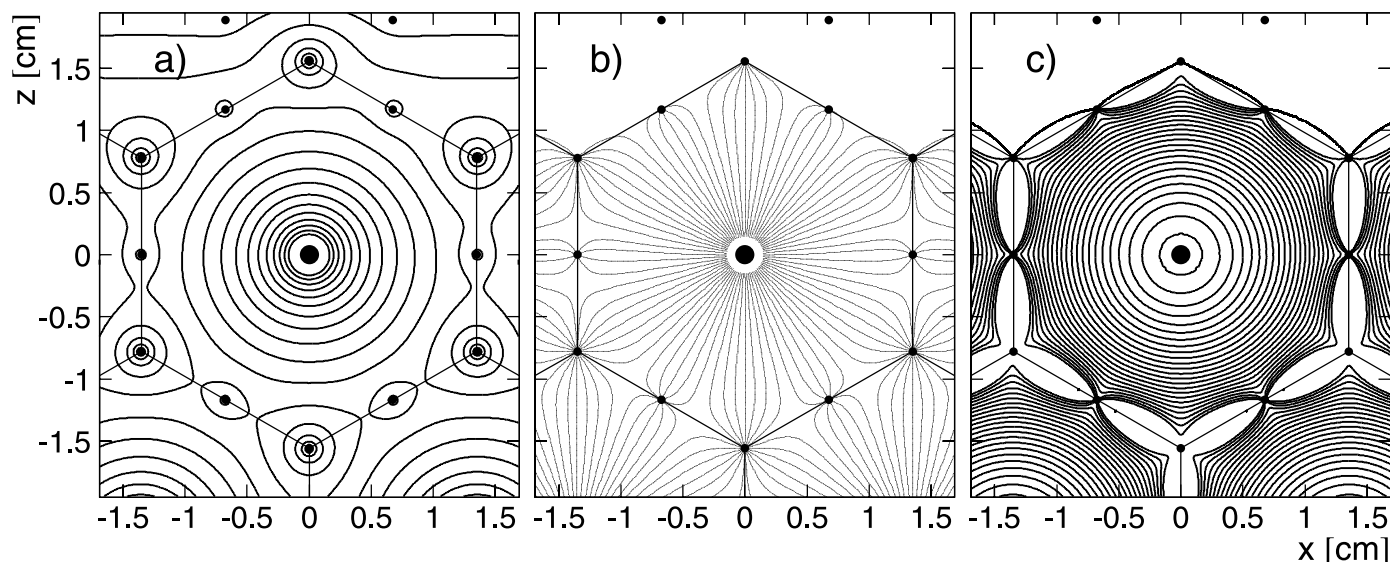


FIG. 2.—Field configuration in a hexagonal drift cell. (a) Lines of equal electric potential. (b) Electric field lines. (c) Lines of equal drift time on 100 ns intervals for ground data setting (see text). The sense wire at the center of the drift cell is surrounded by grounded cathode wires located in the corners of the hexagon and intermediate additional potential wires.

(G10). A low-grammage window (125 μm Mylar and 35 μm copper) mounted on the top and bottom edges of the chamber wall closed the detector volume.

The distance of the particle track to the sense wire of a penetrated cell was determined by measuring the drift time of the liberated electrons with respect to a well-defined system trigger. The drift time of each sense wire was measured with a LeCroy 4290 time-to-digital converter (TDC) with a least count of 3 ns. Each sense wire signal was analyzed by a charge-sensitive amplifier and a discriminator. The time measurements were operated in common-stop mode; e.g., all sense wire time measurements were stopped 4 μs after the system trigger was issued. The time measurement started individually when a sense wire signal exceeded the threshold of the discriminator. Further details on the magnetic rigidity spectrometer are reported by Hams et al. (1999, 2001).

2.2. Time-of-Flight System

The TOF system provided a measurement of the particle velocity and a redundant charge determination. In addition, the TOF was used to provide the system trigger for the instrument. The TOF detector was composed of three 1 cm thick layers of fast Bicron BC420 with a rise time of 0.5 ns. The separation from the top-to-middle and top-to-bottom scintillator layers was 206.8 and 260 cm, respectively. The top and bottom TOF plane consisted of five scintillation paddles, each with a total cross section area of 100 cm \times 100 cm per plane. The middle scintillator located under the bottom DC consisted of three paddles and had a total area of 66 cm \times 66 cm. Each paddle was individually wrapped in black tape and viewed from both ends with fast 2 inch Hamamatsu R2083 photomultiplier tubes (PMTs). The nominal rise time of the PMT anode signal was 0.7 ns. Adiabatic acrylic light pipes adapted the rectangular cross section of the scintillator to the round photocathode of the PMT.

The TOF PMTs were operated at negative HV. The anode signal of each PMT was split for amplitude and timing deter-

mination. To improve the time resolution of the TOF, a dual-threshold discrimination was employed. In flight, the lower threshold for the primary time measurement was set to 10% of the nominal amplitude of a beryllium event. The second threshold, which was used for the system trigger, was set to 50% of the nominal beryllium event. To allow for amplitude-dependent corrections in the rise time (time walk), the signals of both thresholds were digitized. An 11 bit LeCroy 2229 TDC system with a nominal least count of 30 ps was used for the time measurement.

For the amplitude analysis of the PMT signal, a charge-sensitive LeCroy 2249A analog-to-digital converter (ADC) with a least count of 0.25 pC was employed. To extend the dynamic range, the analog signal of each PMT was split in a 1:16 ratio and analyzed by two LeCroy 2249A (10 bit) modules, resulting in an effective 14 bit resolution for the charge separation.

2.3. Cerenkov Counters

Two light-diffusion aerogel CK counters provided an extended measure of the velocity beyond the TOF range useful for determining mass ($\sim 1 \text{ GeV nucleon}^{-1}$ for beryllium). Each counter contained two layers of silica-aerogel blocks (each 38 cm \times 38 cm \times 2 cm) arranged in a 2 \times 2 matrix. The Cerenkov light in each detector was viewed by 16 Hamamatsu R1848 3 inch PMTs. The PMTs were selected for good single-photoelectron resolution. To achieve homogeneous Cerenkov light diffusion, each counter was lined with highly reflective Tyvek. The signal of each PMT was fed to a charge-sensitive Amptek-203 preamplifier with a high- and low-gain output. Both outputs were digitized by a LeCroy 2259B ADC with an 11 bit dynamic range.

The choice of the radiator material determines the threshold for Cerenkov light production and thus the energy range for the velocity measurement. In the 1998 flight these counters were each equipped with a silica-aerogel radiator with a nominal index of refraction n of 1.14, resulting in an energy threshold of $1.01 \text{ GeV nucleon}^{-1}$. Further details on the

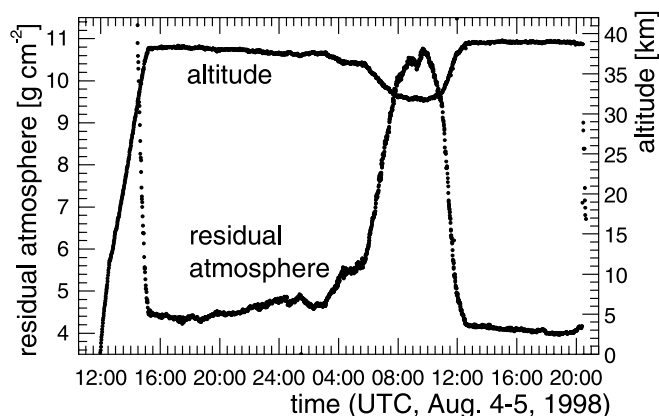


FIG. 3.—ISOMAX 1998 flight profile.

CK counters can be found elsewhere (de Nolfo et al. 1999, 2001).

3. FLIGHT AND DATA-TAKING

3.1. Flight

ISOMAX was launched for the first time on the morning of 1998 August 4 from Lynn Lake, Manitoba, Canada. The experiment reached a float altitude of 36 km roughly 3 hr after launch. Ascent data transmitted via telemetry was used to optimize the detector settings for beryllium ($Z = 4$) and to suppress the abundant protons and some of the relativistic helium. Figure 3 shows the ISOMAX flight profile. For 13 hr of the 29 hr flight, ISOMAX was optimized for the detection of beryllium and remained at a residual atmosphere of less than 5 g cm^{-2} . As can be seen in Figure 3, on the early morning of August 5 the instrument drooped to 31 km (10 g cm^{-2}) while flying over a thunderstorm. During the time that the instrument lost altitude, the ambient temperature inside the pressure vessel dropped by 20°C to -8°C . We will address the affects of the temperature drop in § 3.2 when we discuss trigger conditions. The ambient temperature inside the gondola increased after the balloon gained altitude again the next morning. The geomagnetic cutoff varied between $0.35 \text{ GV } c^{-1}$ at launch and $0.65 \text{ GV } c^{-1}$ at the completion of the flight. At the end of the flight, the instrument was recovered in excellent condition near Peace River, Alberta, Canada.

3.2. Trigger and Data-taking

Data was processed with the start of the first-level trigger. The first-level trigger was derived from a coincidence at the top and middle TOF scintillators. A TOF layer was considered hit with the registration of at least one PMT signal (high threshold; § 2.2) on either side of this scintillator plane. The aperture of the outer scintillator planes used for the first-level trigger did not restrict particles to penetrate the middle tracking detector. Events fulfilling the first-level trigger condition but missing the middle DC have a lower tracking resolution. A second-level trigger was imposed to obtain high-accuracy track reconstruction in the uniform, high-field region of the magnet. The second-level trigger restricts particle tracks to the sensitive volume of the middle DC by requiring at least one drift-cell hit in either of the two outermost top layers and at least one drift-cell hit in either of the two outermost bottom layers of the middle DC in the bending as well as nonbending planes. The second-level trigger condition was derived from

the fast hit register in the TDCs of the middle DC. If the second-level trigger condition was fulfilled, the event was processed and stored in the data stream. The geometry factor of the instrument was $450 \text{ cm}^2 \text{ sr}$ for particles with a rigidity R greater than $1 \text{ GV } c^{-1}$ that penetrated the sensitive area of the three-layer TOF and all DC layers. The instrumental aperture is independent of energy for the ranges of energy considered in this study.

Shortly before reaching float altitude, the instrument settings were optimized for beryllium. The HVs for the TOF and CK counters were lowered to increase the dynamic range of the ADCs and thus encompass elements from lithium to oxygen. The sense wire HV in the DC was lowered to improve the sensitivity of the drift cells to beryllium. In flight, we used the total number of hit drift cells per event, requiring on average one hit per layer for lithium, beryllium, and boron, as a measure of sensitivity. In addition, the HV for the additional potential wires was adjusted to maintain a high cylindrical symmetry of the electric field in the drift cells (Fig. 2). Finally, the discriminator threshold of the TOF, deriving the first-level trigger (see § 2.2), was raised to suppress most of the abundant proton and part of the relativistic helium events. The second threshold of the TOF, used only for timing, remained unchanged.

Because of the limited bandwidth in the telemetry and the variable number of DC data words, the flight computer rejected those events that had an excessive number of DC hits. The number of hits at which an event was not recorded was roughly 3 times the number of DC hits for an average beryllium event. With our DC HV setting for beryllium, we obtained full efficiency for elements from helium to carbon with only a negligible amount of rejected oxygen, despite the limitation in processing events with large DC hit numbers.

While flying over a thunderstorm (see § 3) the instrument's ambient temperature dropped rapidly and caused a failure in the HV supply for the additional potential wires of the DC. This failure resulted in an increased effective potential on the sense wires and thus, on average, an elevated number of DC hits. For the sake of instrument stability during the remainder of the flight, we decided to leave the HV on the sense wires unchanged. Although an increased number of DC hits were observed, ISOMAX was able to collect an unbiased data set for the elements lithium through boron and in particular the scientifically interesting beryllium events.

4. DATA ANALYSIS

4.1. Magnetic Rigidity Spectrometer

The magnetic rigidity spectrometer measures the curvatures of trajectories for charged particles passing through the magnetic field in the DC. The track curvature is proportional to the particle's rigidity, R . Charged particles passing through the DC drift cells ionize the gas within the cells, liberating electron-ion pairs along the particle trajectory. The ensemble of hit drift cells is subsequently used to reconstruct the particle trajectory. The transit time for liberated electrons, i.e., the drift time, provides a measure of the distance of closest approach of the passing particle to the sense wire for hit cells. The relationship between drift time and the distance of closest approach is referred to as the path-to-time relation (PTR) and was revised from the predecessor of ISOMAX, IMAX (Hof et al. 1994; Golden et al. 1991), to suit the current configuration. The PTR is optimized iteratively for each individual charge. The corresponding distance for a given drift time

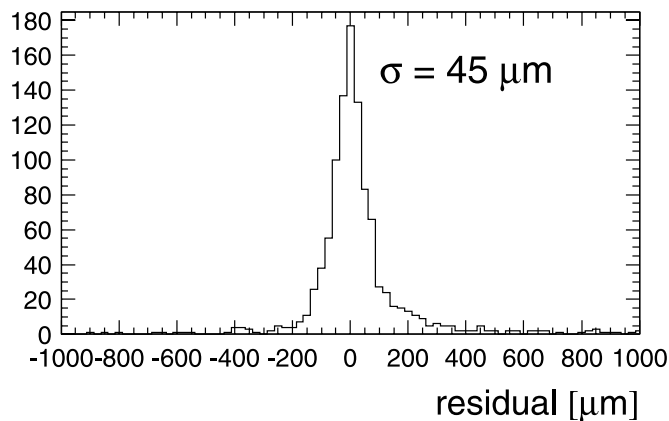


FIG. 4.—Histogram of residuals for beryllium in the central drift region of 0.3–1.0 cm. The spatial resolution is 45 μm .

differs by less than 100 μm for all charges considered in this study. The symmetry of the electric field in all drift cells allows the use of one single PTR for a given charge, particle incident angle, and drift time. For trajectories with drift times of less than $\sim 1.7 \mu\text{s}$, which corresponds to the majority of the cell volume, the PTR is relatively independent of incident angle. However, the PTR differs by no more than 300 μm from the nominal small-angle PTR for events with large drift times and large incident angles. The best spatial resolution of the DCs is obtained by accounting for the dependence of the PTR on incident angle and particle charge.

Using in-flight data, the DCs demonstrated a spatial resolution of 54 μm for helium and 45 μm for beryllium, respectively, for particles with $\beta > 0.6$. Figure 4 shows the histogram of residuals, reflecting a spatial resolution for beryllium in the central drift path region of 0.3–1 cm.

The quality of the spectrometer can be characterized by the magnetic field strength and the precision of the tracking detector and is given by the maximum detectable rigidity (MDR) distribution. The MDR is the rigidity for which the relative uncertainty of the rigidity becomes 1 ($\Delta R/R \sim 1$). Figure 5 shows the resulting MDR distribution for in-flight helium. The entries for the shown MDR distribution are computed for each event, incorporating the actual track geometry, including the location and resolution of the measured track positions and the magnetic field integral. The nearly Gaussian shape of the MDR distribution is the result of the magnetic field homogeneity within the tracking detector volume. For the flight configuration of the superconducting spectrometer, the most probable MDR for helium was $0.97 \text{ TV } c^{-1}$, and $1.2 \text{ TV } c^{-1}$ for beryllium.

4.2. Time-of-Flight System

The TOF system determines the particle velocity by measuring the flight time between the top and bottom scintillator planes of the TOF. A timing resolution can be determined separately for each paddle. For each paddle, an effective light propagation speed is derived by comparing the projected particle track from the DC into the paddle and the measured time difference between the detection of the light signal on either end of the paddle. Figure 6 shows in the left panels for in-flight helium and carbon the correlation of the penetration point as determined by the DC versus the time difference measured in one of the paddles of the TOF. The spread in the correlation, as shown in the right panels of Figure 6, between

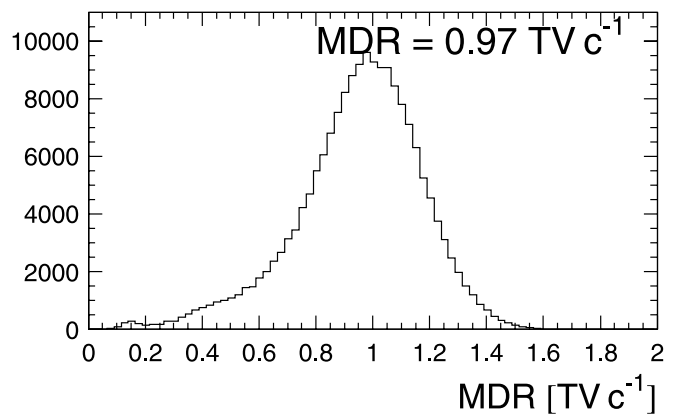


FIG. 5.—Histogram of MDR distribution computed for fast helium events. We obtained a most probable MDR of $0.97 \text{ TV } c^{-1}$ for helium.

expected track position and the measured time difference in a scintillation paddle reflects the single-paddle timing resolution. All TDCs were calibrated in a magnetic field configuration expected during the flight using a programmable pulse generator (Gupta et al. 1997). By using an averaged single-paddle time resolution in each of the outer TOF planes, the TOF time resolution, relevant for the velocity determination, was 70 ps for helium and 60 ps for beryllium (Göbel et al. 2001). The relative uncertainty in the timing resolution determines the relative uncertainty in the velocity. The computed velocity from the TOF accounts for the energy loss of the penetrating particle and thus represents the particle velocity within the middle DC.

The charge is determined from the ADC signals in each of the three TOF planes in conjunction with the velocity measurement of the TOF. The three scintillator layers enable three independent charge determinations, thus significantly improving the charge resolution. In Figure 7 the charge separation in the middle TOF scintillator is shown. The energy loss dE in the figure was derived from a geometric mean of the ADC values of a hit paddle. The two ADC readings were corrected for the incident angle and light attenuation within the scintillator. The velocity β_{12} was derived with the top and middle TOF planes. The solid lines shown in Figure 7 are fits to the separate charge bands, after eliminating events with poor charge reconstruction in the other two TOF layers. A charge scale for each scintillator was derived from the results of these fits. Figure 8 shows a histogram along charge bands for the top scintillator with a 3σ cut on the charge in the other two scintillators and $\beta > 0.5$. As can be seen, the charge resolution for helium through carbon was better than 0.2 charge units. A similar charge resolution was found for the other two TOF planes. This stringent resolution in the TOF layers significantly suppressed the possibility of charge misidentification and a subsequent wrong mass assignment of the particle according to equation (1).

4.3. Cerenkov Counters

The CK counters provide a velocity measurement for particles with energies above $1.01 \text{ GeV nucleon}^{-1}$, corresponding to a threshold for aerogel with an index of refraction of 1.14. The uncertainty in the velocity measurement predominantly depends on the number of photoelectrons (PEs), the ability to distinguish between single and multiple PE events, and the light-yield properties of the aerogel as a function of position.

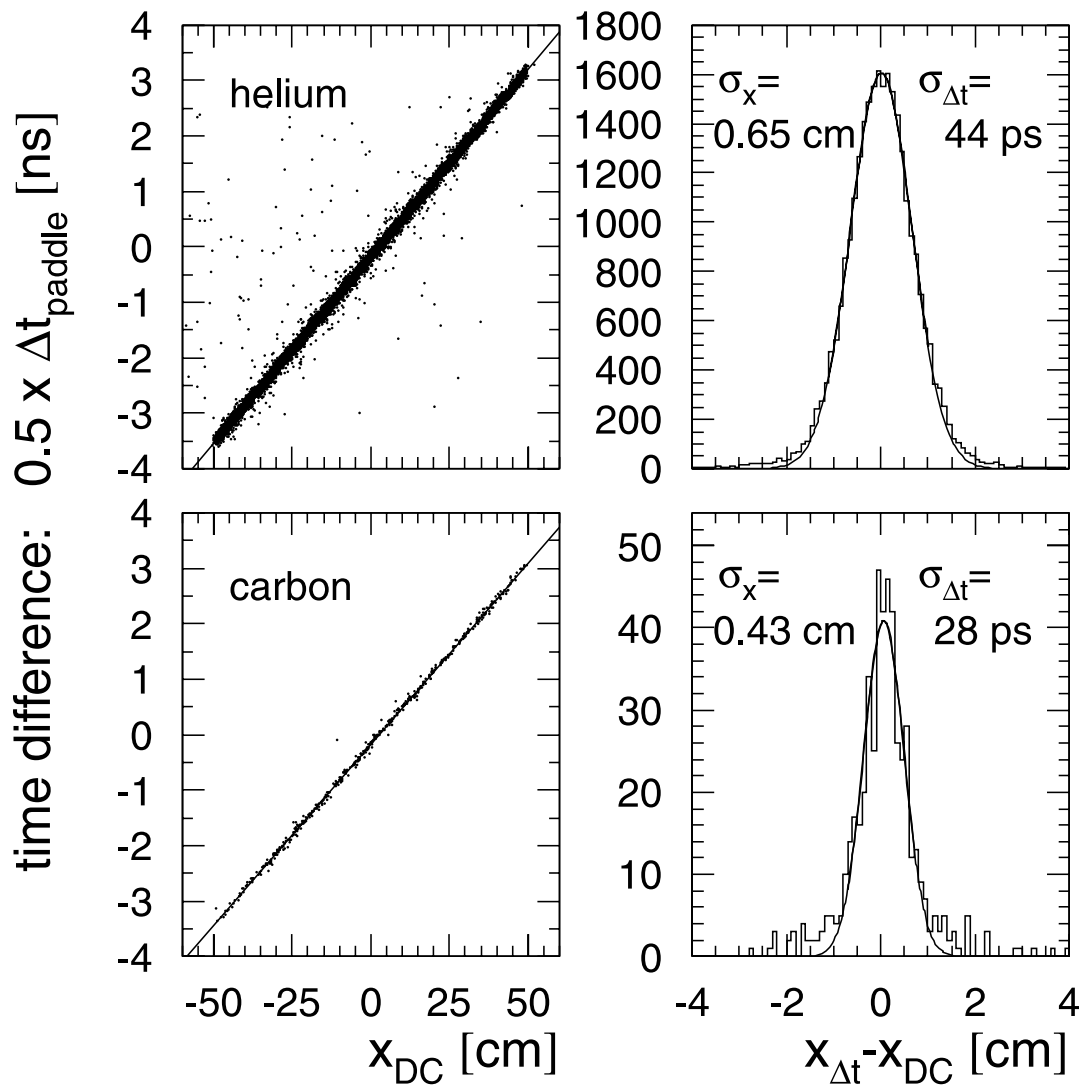


FIG. 6.—Single-paddle time resolution for helium and carbon. *Left:* Measured time difference in the paddle vs. penetration point by the DC. *Right:* Histogram of the time resolution.

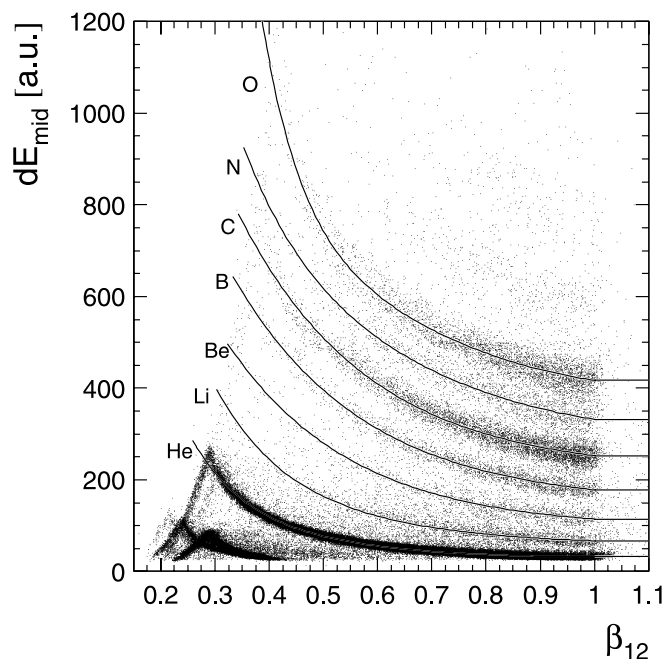


FIG. 7.—Scatter plot of energy loss dE in the middle scintillator vs. particle velocity β_{12} determined from the top and middle TOF panels. Superposed are the derived charge-band fits used for further analysis.

Figure 9 shows a histogram of the raw ADC signals of in-flight helium, as viewed by a typical PMT in the CK counters. As can be seen in the figure, the one- and two-PE peaks are clearly separated. A downhill simplex (amoeba) fit to the PE peaks (*dashed lines*) establishes a correspondence between the PE number and the ADC channel. The total light yield for one CK counter is determined by summing the number of PEs for all 16 PMTs on a given counter. For relativistic single-charged particles, both counters observed a nominal total of 22 PEs (de Nolfo et al. 1999) using 48 hr of preflight muon data. The total number of PEs was also verified with in-flight helium data. In addition, both preflight muon data and in-flight helium data were used to determine the total light yield (i.e., response) as a function of particle position for the aerogel radiators in both counters. The response map for in-flight helium events in the

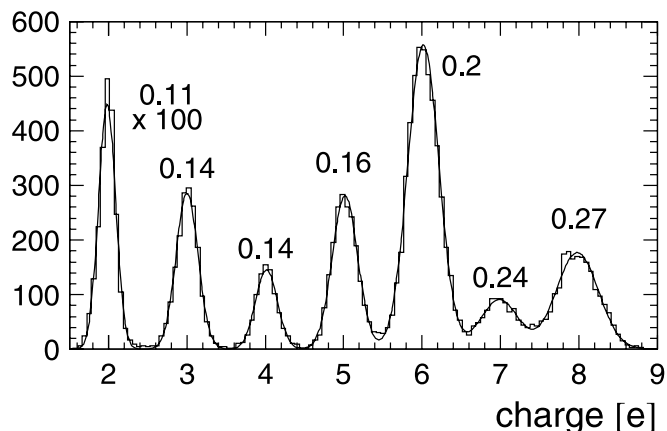


FIG. 8.—In-flight charge separation in the middle TOF obtained by requiring a 3σ cut on charge in the other two scintillators and $\beta > 0.5$. The values close to the charge peaks quote the charge resolution, which is better than 0.2 charge units for He–C.

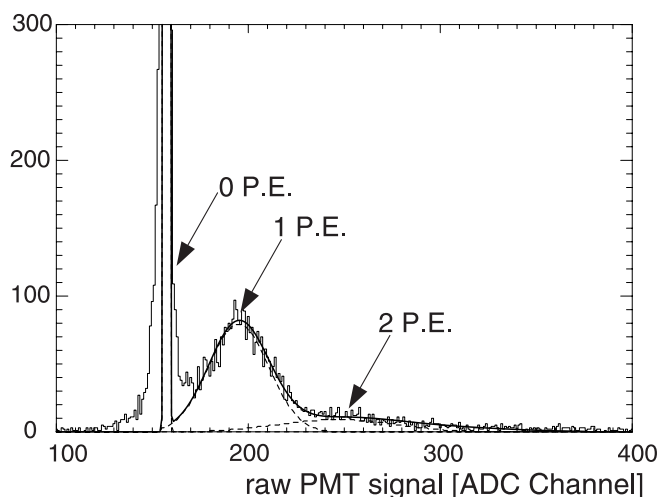


FIG. 9.—Typical Cerenkov ADC raw signal of in-flight helium seen by one PMT. The first and second PE peaks (*dashed lines*) above the pedestal are clearly separated.

upper CK counter is shown in Figure 10. The 2×2 configuration of the aerogel blocks is clearly visible. The total light yield varied by less than 20%, with the largest variations occurring toward the edges of the aerogel blocks.

The velocity is derived from the particle charge, the total number of PEs measured, and the index of refraction of the radiator. Several techniques were used to determine the index of refraction of each aerogel block. The index of refraction is proportional to the radiator density (Poelz & Riethmüller 1982). Prior to the flight the density and corresponding index of refraction were determined for all radiator blocks. In addition, using flight data, the assumed index of refraction of penetrated radiator blocks was varied until a Gaussian fit to the peaks of the reconstructed mass histograms for helium events resulted in peak locations corresponding to the isotopic helium

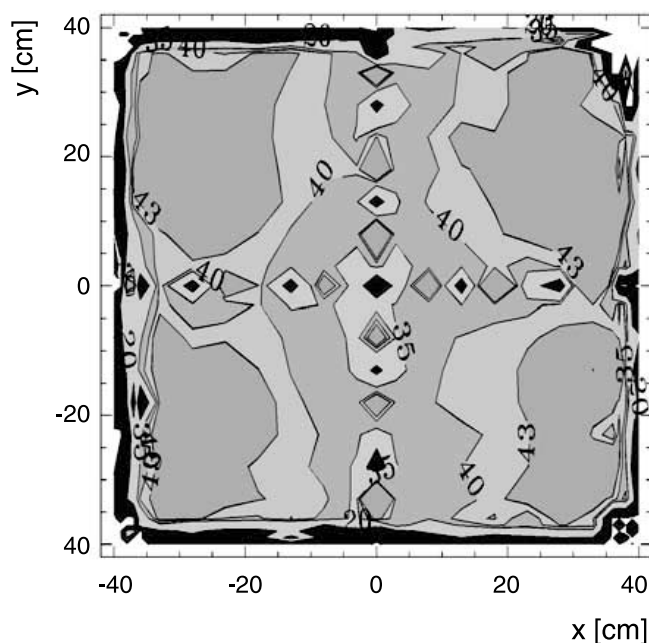


FIG. 10.—Response map for in-flight helium in the upper CK counter. The 2×2 arrangement of the aerogel blocks is clearly visible.

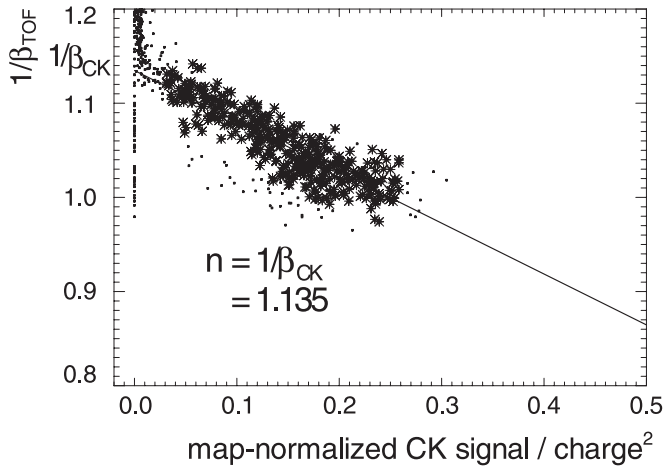


FIG. 11.—Index of refraction for one aerogel block derived from even charge number beryllium, carbon, and oxygen events in conjunction with the TOF. The map-normalized signal was scaled to the charge square.

masses at 3 and 4 amu. Finally, the refractive index was determined by fitting a straight line to the velocity obtained from the TOF system ($1/\beta_{\text{TOF}}$) versus the map-normalized light yield from a particular layer (consisting of two blocks, one on top of the other). Figure 11 shows the reciprocal velocity determined by the TOF versus the total light yield of one two-block layer located in the lower CK counter for beryllium, carbon, and oxygen. Although fewer in number, Be, C, and O nuclei have a greater light yield ($\propto Z^2$) and thus an improved velocity resolution compared with helium events. As shown in Figure 11, the y-intercept of a straight-line fit to the data determines the refractive index. These fits were performed for all four two-block layer sets in each of the two counters. The difference from using He to map the refractive index rather than Be, C, and O events is less than 0.3%. Block-to-block variations in the refractive index are less than 5% and have been accounted for in the velocity determination.

5. DATA SELECTION AND MASS HISTOGRAMS

In order to determine the relative isotopic ratios for beryllium, several selection criteria were applied to the flight data to obtain a clean data sample. To reduce the effects of atmospheric interaction (see § 7), only events recorded at less than 5 g cm^{-2} residual atmosphere were considered for the analysis. After restricting the altitude, roughly 13 hr of flight data remained (see Fig. 3). For the rigidity measurement, a successful track reconstruction in the DC requires at least eight hit layers in the bending plane N_x and at least four layers in the nonbending plane N_y , with the restriction that all multitrack events are rejected. Excellent charge resolution is obtained by requiring a consistent measure of charge in all three TOF layers. Specifically, for beryllium a cut requiring $|Z_i - 4| \leq 0.5$ charge units was imposed, where i denotes the different scintillator layers. This criteria ensures that the contamination to beryllium from events with misidentified charge is less than 10^{-6} . A cut of 0.5 charge units corresponds to a $\sim 3 \sigma$ charge resolution. In addition, only events with a single-paddle hit in each layer were used for further analysis.

The velocity of incident particles in the TOF regime, from 0.2 to $1 \text{ GeV nucleon}^{-1}$ for beryllium, was determined from the top and bottom scintillator arrays. We account for energy losses within the instrument and the subsequent increase in

TABLE 1
CUTS APPLIED FOR DATA SELECTION AND ENERGY RANGES FOR THE
TIME-OF-FLIGHT AND CERENKOV COUNTERS

Parameter	Value
Cuts ^a	
ρ_{alt}	$\leq 5 \text{ g cm}^{-2}$
DC single-track fit.....	$N_x \geq 8, N_y \geq 4$
$ Z_i - 4 $	$\leq 0.5 e$ for all $i \in [\text{top, middle, bottom}]$
TOF Energy Range	
$Z = 3$	$0.15 \text{ GeV nucleon}^{-1} \leq E_{\text{kin}} \leq 1.3 \text{ GeV nucleon}^{-1}$
$Z = 4$	$0.20 \text{ GeV nucleon}^{-1} \leq E_{\text{kin}} \leq 1.0 \text{ GeV nucleon}^{-1}$
$Z = 5$	$0.20 \text{ GeV nucleon}^{-1} \leq E_{\text{kin}} \leq 0.9 \text{ GeV nucleon}^{-1}$
CK Energy Range ^b	
$Z = 4$	$1.1 \text{ GeV nucleon}^{-1} \leq E_{\text{kin}} \leq 2.0 \text{ GeV nucleon}^{-1}$

^a Single-paddle hit in TOF layer i .

^b Cut on response map variation.

local dE/dx . In the energy range $1.1\text{--}2 \text{ GeV nucleon}^{-1}$, the two CK counters were used to determine the velocity. A geometric cut was imposed to accept only events in the Cerenkov regime that had penetrated the blocks within an active area of uniform aerogel response for both counters. By requiring a response-map variation of 7% or less, the total active area was reduced to 66%. The energy ranges considered in this study are selected to optimize mass resolution. For this flight configuration, the mass resolution of the light isotopes in the TOF-rigidity and Cerenkov-rigidity techniques is dominated by the uncertainty in the velocity determination. For ^{10}Be the energy intervals above represent an uncertainty in mass identification of better than 0.25 amu. The selection criteria used in this analysis are summarized in Table 1.

Figure 12 represents the mass histograms extracted from the flight data by using the selection criteria outlined in Table 1. Figures 12a–12c show the resulting mass identification with the TOF-rigidity technique for (a) lithium, (c) beryllium, and (b) boron. In addition, Figure 12d shows the mass histogram for beryllium using the Cerenkov-rigidity technique for mass determination. Also shown in the figure are least-squares fits to the mass histograms, which are subsequently used to derive the relative isotopic abundances. We note that the short-lived isotopes ^8Li and ^{12}B are present in the data. These isotopes are produced by interactions in the atmosphere above the instrument. In addition to a combined energy bin for lithium and boron, sufficient statistics allow the data for lithium and boron to be separated into two energy bins, as is shown in Figure 13. After applying the above selection criteria, 424 beryllium events remained in the TOF energy range and 94 beryllium events remained in the Cerenkov energy regime. The isotopic ratio $^{10}\text{Be}/^9\text{Be}$ is 0.249 ± 0.046 in the TOF range from 0.2 to $1 \text{ GeV nucleon}^{-1}$ and 0.349 ± 0.125 in the Cerenkov range from 1.1 to $2 \text{ GeV nucleon}^{-1}$. Table 2 shows the isotopic ratios for lithium to boron for each energy range.

6. INSTRUMENT EFFICIENCIES

The detection efficiencies have been accounted for separately for each subsystem. As mentioned above, the charge selection requires a consistent measure of charge in all three TOF paddles, which results in an overall efficiency for charge determination of 94%.

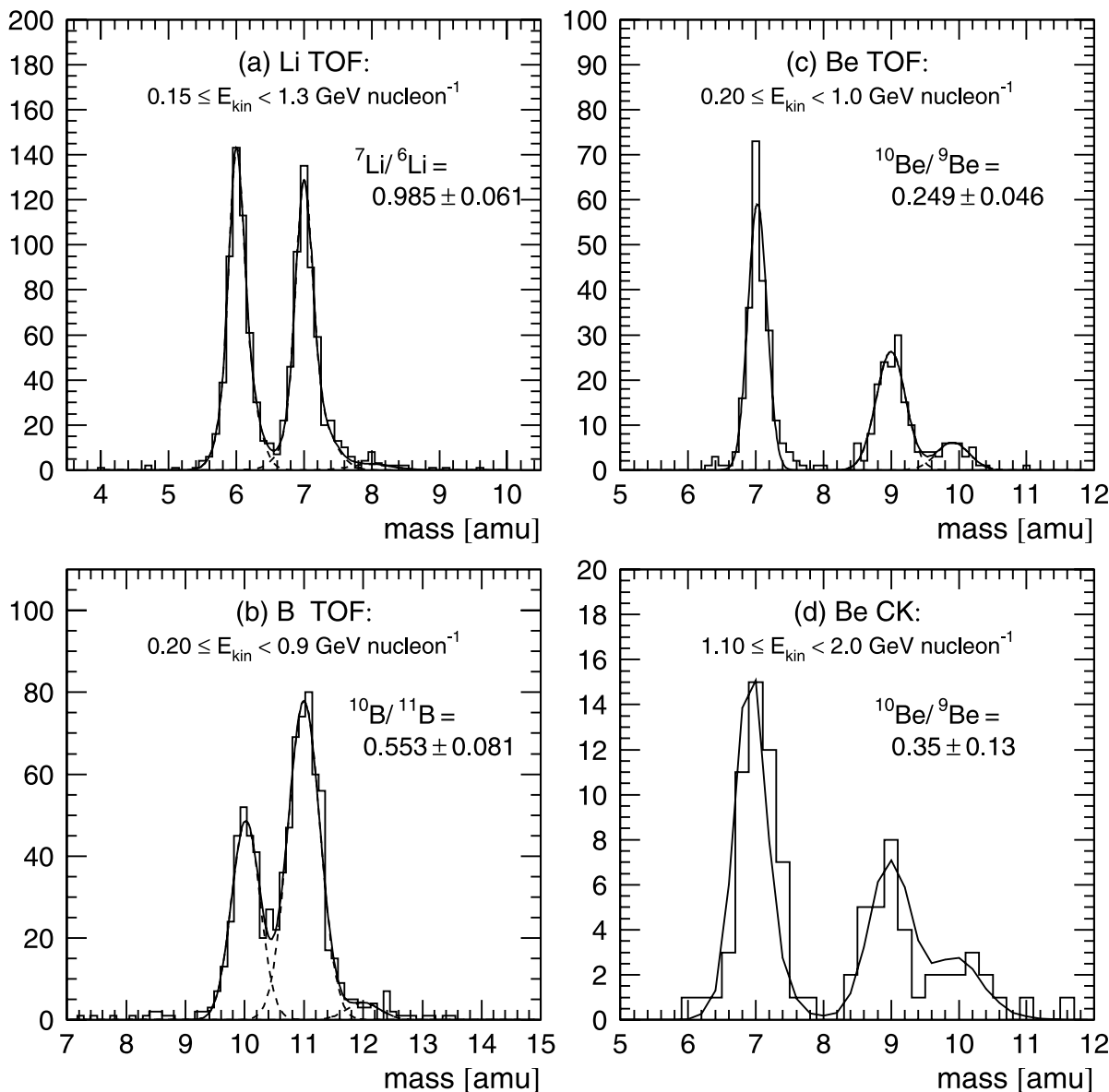


FIG. 12.—Mass histograms for the isotopes of (a) lithium, (b) boron, and (c, d) beryllium (TOF and CK, respectively). The solid lines represent the fitted isotopic ratios also shown in the plot.

The DC tracking efficiency is defined as the ratio of events satisfying the DC tracking cuts to the number of events selected using criteria based only on the TOF. For the DC tracking efficiency, the TOF was used to select events that were fully contained in the DC. In addition, the charge and velocity were calculated without relying on further refinements from the DC, thus enabling the determination of the tracking efficiency as a function of charge and energy. The track reconstruction efficiency for each element was separately investigated for both flight parts, i.e., with and without additional potential wires HV (see § 3.2). No rigidity dependence was found in the cuts discussed above for the light elements in the relevant energy range for both parts of the flight. For beryllium the DC tracking efficiency was 94%.

Ground muon data ($Z = 1$) recorded prior to the flight and without a second-level trigger (§ 3.2) have shown that the event rate changes by introducing a second-level trigger. For ground data, the efficiency for registering the penetration of a typical drift cell is 97%. The high drift-cell efficiency means

that applying a second-level trigger predominantly affects the instrument aperture. During the flight, the effects of the second-level trigger may depend on charge and particle energy as well. We compared the preflight drift-cell efficiency with the cell efficiency in the flight data for those layers not comprising the second-level trigger condition. We found in the first part of the flight for the elements lithium through oxygen a drift-cell efficiency of 97% throughout the relevant drift paths in the cell, whereas helium events show an efficiency that decreases significantly with increasing drift-cell radius. The DCs for this flight were optimized for a beryllium measurement, resulting in a reduced efficiency for helium due to the decrease in ionization with decreasing charge. Accounting for the high drift-cell efficiency during the flight, the effects of the second-level trigger on charge can be neglected for elements lithium and higher. In addition, the drift-cell efficiency shows no energy dependence over the entire energy range considered in this study. For the second part of the flight, where the DC sense wire HV was effectively increased, the drift-cell efficiency is

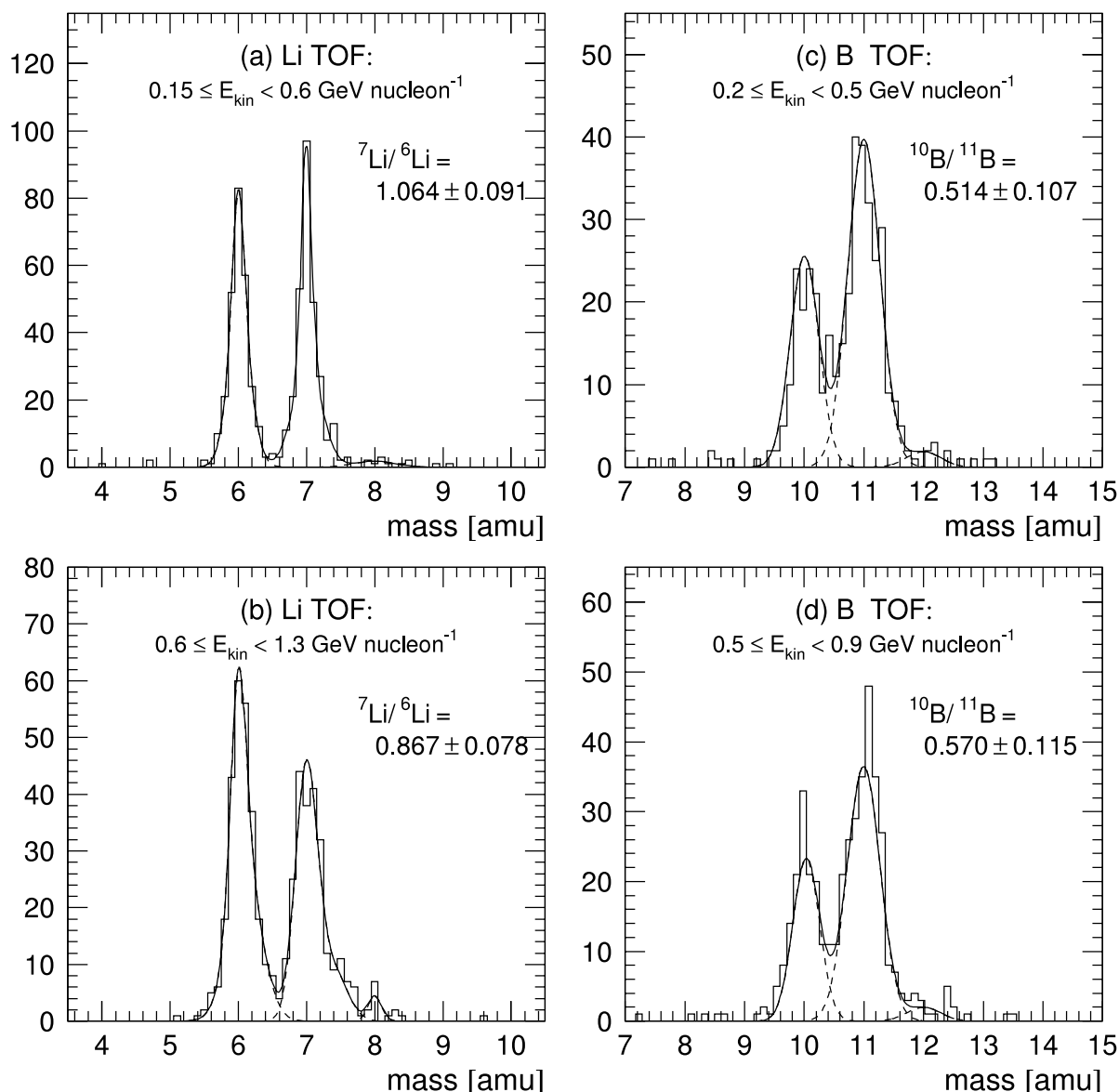


FIG. 13.—Mass histograms with the TOF for the isotopes of lithium and boron in two energy ranges. The solid lines represent the fitted isotopic ratios also shown in the plot.

effectively increased, resulting in an even smaller dependence on the second-level trigger.

7. INSTRUMENTAL AND ATMOSPHERIC CORRECTION

The isotopic ratio as measured in the instrument and discussed in § 5 requires further corrections for interactions within the instrument and atmosphere. The flux of cosmic-ray particles propagating through the residual atmosphere above the instrument may interact with the air molecules. Consequently, the particle flux can suffer energy losses and fragmentation. Fragmentation products of heavier elements contribute to beryllium isotopes. Beryllium isotopes also interact with the atmosphere and suffer fragmentation losses. Both processes have an effect on the isotopic ratio. In addition, similar interactions in the instrument have to be considered.

The total grammage of the entire instrument stack is 11.2 g cm^{-2} . Elements heavier than beryllium that interact in the detector stack are rejected by the requirement for charge consistency in all three TOF layers and the single-track

requirement in the DC. The interaction losses within the instrument are determined assuming the parameterization for inelastic cross sections of Kox et al. (1987). For beryllium $^{10}\text{Be}/^9\text{Be}$, the instrumental correction is 1.038.

In addition to the instrumental interactions, a correction must be applied for interactions of the cosmic rays with the residual atmosphere above the instrument. The particles have penetrated on average 4.6 g cm^{-2} before reaching the instrument, assuming an average particle zenith angle of 15° .

Understanding the effects of the atmosphere on the measured isotopic ratios at balloon altitudes requires knowledge of the primary cosmic-ray spectra. The interstellar spectra from boron to nickel were derived from observations of the CRIS instrument on the spacecraft (Davis et al. 2000) and the *HEAO 3* satellite (Engelmann et al. 1990). The measured elemental spectra at the low energies from CRIS observations and at higher energies from *HEAO 3* were parameterized and demodulated with a solar modulation parameter consistent with that experienced by *ACE* and *HEAO 3*. The interstellar spectra

TABLE 2
MEASURED ISOTOPIC RATIOS OF LITHIUM, BERYLLIUM, AND BORON

INSTRUMENT		TOP OF INSTRUMENT		TOP OF ATMOSPHERE	
Energy	Ratio \pm Statistical	Energy	Ratio \pm Statistical	Energy	Ratio \pm Statistical \pm Systematic
TOF: $^{10}\text{Be}/^9\text{Be}$					
0.200–1.000.....	0.249 ± 0.046	0.232–1.017	0.259 ± 0.048	0.257–1.031	$0.195 \pm 0.036 \pm 0.039$
CK: $^{10}\text{Be}/^9\text{Be}$					
1.100–2.000.....	0.349 ± 0.125	1.117–2.015	0.363 ± 0.130	1.131–2.030	$0.317 \pm 0.109 \pm 0.042$
TOF: $^7\text{Li}/^6\text{Li}$					
0.150–1.300.....	0.985 ± 0.061	0.180–1.313	1.034 ± 0.064	0.204–1.324	$1.058 \pm 0.065 \pm 0.146$
0.150–0.600.....	1.064 ± 0.091	0.180–0.615	1.117 ± 0.096	0.204–0.628	$1.149 \pm 0.099 \pm 0.158$
0.600–1.300.....	0.867 ± 0.078	0.615–1.313	0.910 ± 0.082	0.628–1.324	$0.930 \pm 0.084 \pm 0.129$
TOF: $^{10}\text{B}/^{11}\text{B}$					
0.200–0.900.....	0.553 ± 0.081	0.245–0.924	0.530 ± 0.078	0.283–0.947	$0.520 \pm 0.076 \pm 0.047$
0.200–0.500.....	0.514 ± 0.107	0.245–0.529	0.459 ± 0.102	0.283–0.556	$0.473 \pm 0.099 \pm 0.048$
0.500–0.900.....	0.570 ± 0.115	0.529–0.924	0.548 ± 0.111	0.556–0.947	$0.544 \pm 0.110 \pm 0.049$

NOTES.—Shown are the measured isotopic ratios of lithium, beryllium, and boron in the instrument and at TOA, together with the respective energy ranges in GeV nucleon^{-1} . The TOA values are the isotopic ratios with statistical and systematic uncertainties. The systematic error gives the combined effect of the atmospheric and instrumental propagations due to cross section uncertainties.

are subsequently modulated with a solar modulation parameter of 430 MV, reflecting the amount of modulation experienced by ISOMAX in 1998. For the elements boron to sodium we also considered the isotopic composition in the cosmic rays (Gibner et al. 1992; Webber et al. 1997) to obtain isotopic spectra. Above Na, we used elemental spectra. In addition, we derived a ^9Be spectra from an LBM ($n = 0.3 \text{ g cm}^{-2}$; A. Molnar 2002, private communication) and assumed a similar spectral shape for ^{10}Be . Similarly, a ^7Li spectra at TOA was obtained from an LBM calculation, which was used for studying the propagation of lithium isotopes through the atmosphere.

For a given beryllium ratio at TOA, we propagated the set of spectra (Be–Ni) through the residual atmosphere and obtained a corresponding beryllium ratio above the instrument. The propagation analysis accounts for energy loss of the particle while penetrating the atmosphere. The partial cross sections

used in the propagation analysis were those of Silberberg et al. (1998) and Tsao et al. (1998). The total inelastic cross sections were derived from Kox et al. (1987).

Figure 14a shows the result of this propagation for beryllium. Displayed are the correlation of the beryllium ratio above the experiment (top of experiment, TOE) versus the ratio at TOA for the two energy ranges of the TOF and CK. At TOA the $^{10}\text{Be}/^9\text{Be}$ ratio was roughly 75% and 88% in the TOF and the CK ranges, respectively. Table 2 lists the isotopic ratios and energy ranges for beryllium. In an analogous fashion we derived an atmospheric correction for the boron and lithium ratios (Figs. 14b–14c). The isotopic ratios for lithium and boron are also included in Table 2.

The cross sections used in the instrumental and atmospheric propagation are subject to uncertainties. We estimated that the total cross sections are known at a 10% level and the partial cross sections at a 30% level. The resulting systematic errors

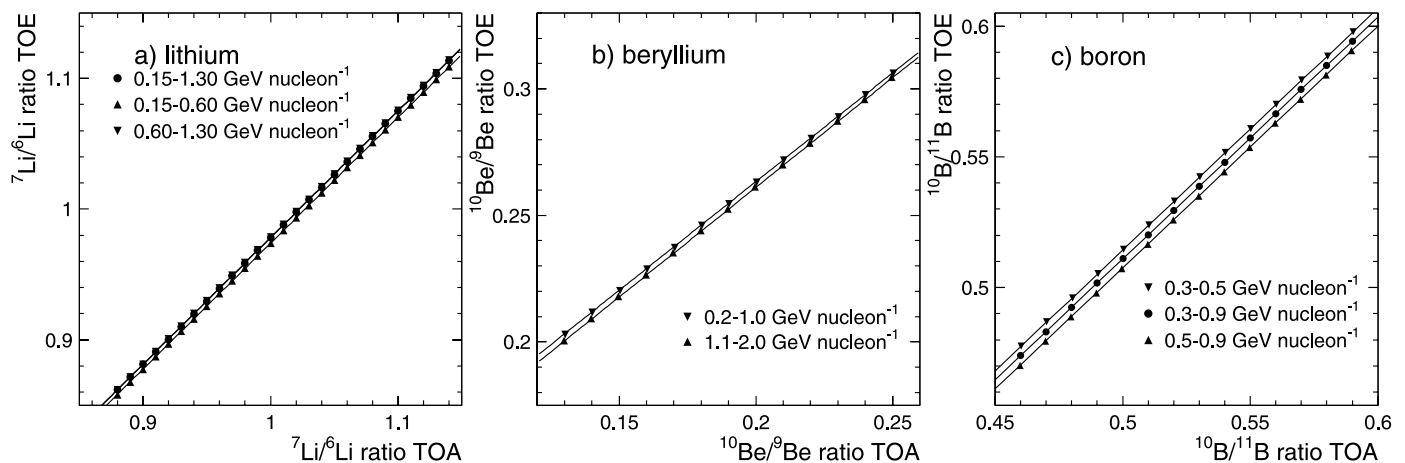


FIG. 14.—(b) Atmospheric correction for beryllium isotopic ratio in the TOF and CK energy ranges, together with the correction for the (a) lithium and (c) boron ratio in the TOF energy range. Both plots display the ratio at TOE vs. the ratio at TOA.

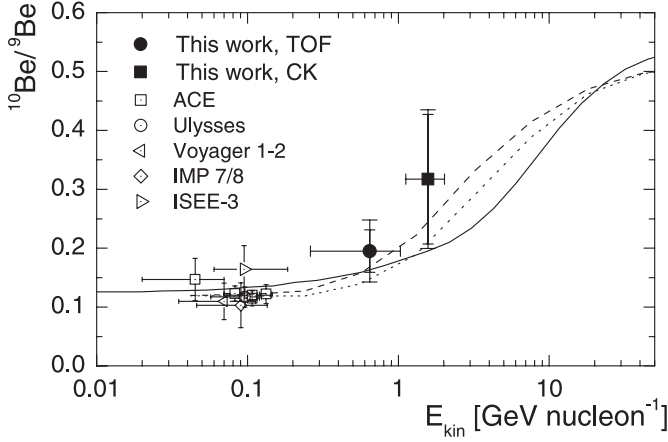


FIG. 15.—Beryllium ratio at TOA of ISOMAX compared with satellite measurements. The lines show the expected beryllium ratio in different propagation models. The solid line represents a prediction in a diffusion-halo model with reacceleration by Moskalenko et al. (2003). The dotted line represents an LBM by Streitmatter & Stephens (2001) with a hydrogen density of $n_{\text{H}} = 0.2 \text{ cm}^{-3}$, and the dashed line represents an LBM in which the solar system is part of a low-density Local Bubble and the remainder of the Galaxy has a higher hydrogen density $n_{\text{H}} = 0.5 \text{ cm}^{-3}$.

in the isotopic ratio due to the uncertainties in the cross section are also summarized in Table 2, where the last column states the combined systematic uncertainty from the atmospheric and instrumental propagation analysis.

8. RESULTS

We obtain a ratio at TOA of $^{10}\text{Be}/^9\text{Be} = 0.195 \pm 0.036(\text{statistical}) \pm 0.039(\text{systematic})$ in the energy range $0.257\text{--}1.031 \text{ GeV nucleon}^{-1}$, and in the energy range $1.131\text{--}2.030 \text{ GeV nucleon}^{-1}$ a TOA ratio of $^{10}\text{Be}/^9\text{Be} = 0.317 \pm 0.109(\text{statistical}) \pm 0.042(\text{systematic})$, determined from the TOF system and the CK counters, respectively. In Figure 15 the two beryllium results of ISOMAX are shown. The error bars in the figure represent the statistical errors of our measurement and the combined uncertainty including systematic uncertainties from the instrumental and atmospheric propagation. The figure also shows the results of satellite measurements at several hundred MeV nucleon^{-1} from *ACE* (Yanasak et al. 2001), *Ulysses* (Connel 1998), *Voyager 1* and

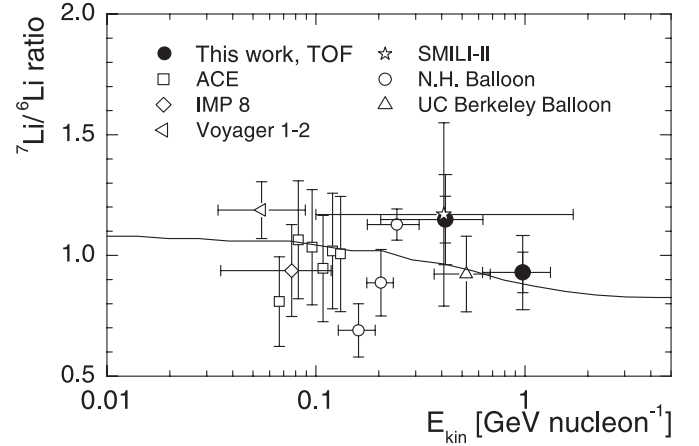


FIG. 17.—Lithium ratio of ISOMAX in the TOF energy range, together with measurements of other experiments: *ACE* (de Nolfo et al. 2003), *IMP 8* (Garcia-Munoz et al. 1975), *Voyager 1* and *Voyager 2* (Webber et al. 2002), *SMILI II* (Ahlen et al. 2000), New Hampshire (Webber & Kish 1979; Webber et al. 1977), and UC Berkeley (Buffington et al. 1978). The solid line represents a prediction in a diffusion-halo model with reacceleration by Moskalenko et al. (2003).

Voyager 2 (Webber et al. 2002), *ISEE 3* (Wiedenbeck & Greiner 1980), and *IMP 7* and *IMP 8* (Garcia-Munoz et al. 1981), as well as model predictions for the beryllium ratio. The dashed line is an LBM by Streitmatter & Stephens (2001) in which the solar system is part of a low-density Local Bubble with a size of 100 pc and a hydrogen density of $n_{\text{H}} = 0.5 \text{ cm}^{-3}$ in the remainder of the Galaxy; the dotted line is an LBM without the Local Bubble and a hydrogen density of $n_{\text{H}} = 0.2 \text{ cm}^{-3}$. The solid curve is a diffusive-halo model by Moskalenko et al. (2003) with a halo size of 4 kpc and reacceleration.

The statistical uncertainties of the ISOMAX results, in combination with the spread in model predictions, preclude any final conclusions concerning cosmic-ray propagation at present. However, it is worthwhile mentioning that the steep increase of the $^{10}\text{Be}/^9\text{Be}$ ratio as measured by ISOMAX is probably difficult to accommodate with the presence of reacceleration, since reacceleration has the general tendency to produce ratios that are below those calculated in the corresponding model without reacceleration.

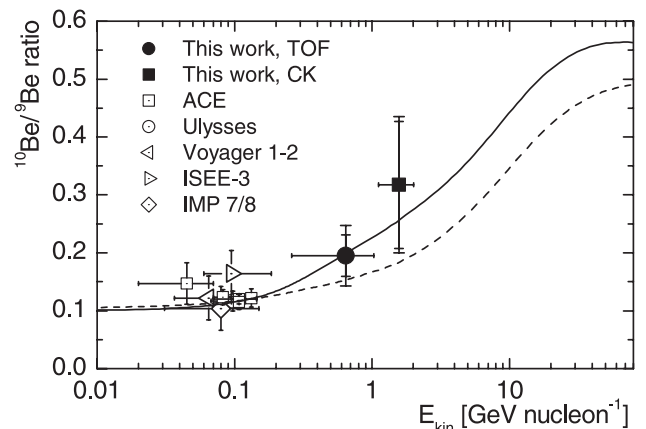
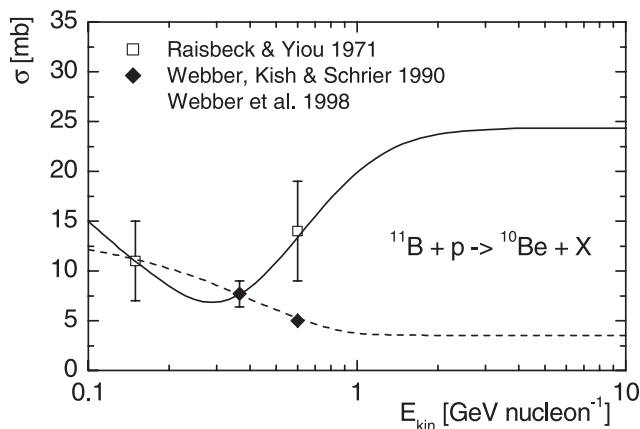


FIG. 16.—Left: Measured fragmentation cross sections of ^{11}B to ^{10}Be of Raisbeck & Yiou (1971) and Webber et al. (1990, 1998) and two parametrizations of the data by the authors. Molnar & Simon (2003) used the two cross section parameterizations to calculate the beryllium ratio in a diffusive halo model. Right: Corresponding resulting beryllium ratios, shown with the same line types.

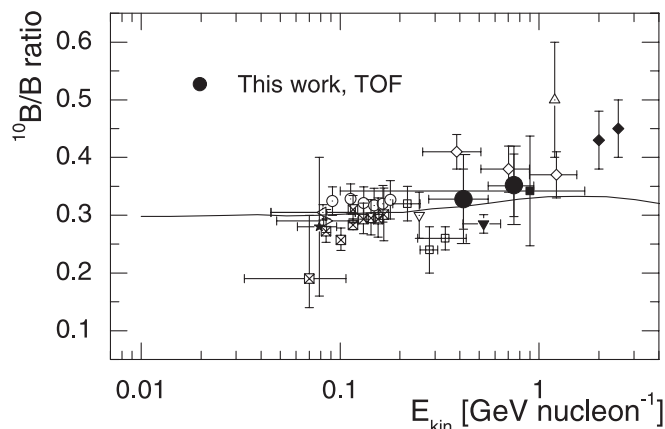


FIG. 18.—Boron ratio of ISOMAX in the TOF regime, together with measurements of other experiments. *Dotted circle*: ACE, de Nolfo et al. (2003). *Dotted left-pointing triangle*: Webber et al. (2002). *Filled square*: Ahlen et al. (2000). *Filled downward-pointing triangle*: Gibner et al. (1992). *Boxed times sign*: Krombel & Wiedenbeck (1988), Mewaldt et al. (1981). *Filled diamond*: Soutoul et al. (1983), Byrnak et al. (1983). *Star*: Smith & McDonald (1981). *Boxed plus sign*: Webber & Kish (1979), Webber et al. (1977). *Open diamond*: Buffington et al. (1978). *Open upward-pointing triangle*: Dwyer (1978). *Dotted downward-pointing triangle*: Hagen et al. (1977). *Dotted right-pointing triangle*: Garcia-Munoz et al. (1977). The solid line represents a prediction in a diffusion-halo model with reacceleration by Moskalenko et al. (2003).

Our beryllium measurement does not confirm the apparent excess of ^{10}Be reported by SMILI (Ahlen et al. 2000). SMILI quoted the detection of nine ^{10}Be in a total of 26 beryllium events at an average energy of $\sim 1 \text{ GeV nucleon}^{-1}$, resulting in a ratio of $^{10}\text{Be}/\text{Be} = 0.35$. Our measured ratio in the instrument covered by the TOF is $^{10}\text{Be}/\text{Be} = 0.09 \pm 0.02$. The SMILI result is more than 10σ higher than our ratio. This low $^{10}\text{Be}/\text{Be}$ ratio is also confirmed by our Cerenkov data.

Within the diffusive-halo model, the steeper than previously predicted increase of the beryllium ratio can also be interpreted as due to an uncertainty in the fragmentation cross section of ^{11}B into ^{10}Be , as discussed in Molnar & Simon (2003). The left panel of Figure 16 shows the existing data of the fragmentation cross section of ^{11}B into ^{10}Be and two possible parameterizations of the data by the authors. The resulting beryllium ratios are shown in the right panel of the figure, when using these two different cross section parameterizations in an otherwise identical diffusive-halo model without reacceleration.

Figures 17 and 18 show the ISOMAX lithium and boron isotopic ratios, respectively, at TOA in the TOF regime. Also included in the figures are predictions of a diffusive-halo model similar to the one used for the beryllium results (Moskalenko et al. 2003) and the results of other experiments (de Nolfo et al. 2003; Webber et al. 1977, 2002; Ahlen et al. 2000; Gibner et al. 1992; Krombel & Wiedenbeck 1988; Soutoul et al. 1983; Smith & McDonald 1981; Webber & Kish 1979; Buffington et al. 1978; Dwyer 1978; Hagen et al. 1977; Garcia-Munoz et al. 1975, 1977).

9. CONCLUSION

The beryllium measurement of ISOMAX is the first of its kind extending the measurement up to $2 \text{ GeV nucleon}^{-1}$. Our data indicate a steep increase in the $^{10}\text{Be}/^{9}\text{Be}$ ratio compared to the ratio measured at a few hundred MeV nucleon^{-1} . Final conclusions on model predictions are not possible with present statistics.

After the first flight in 1998, ISOMAX was equipped with a new low-power data acquisition system to increase the total flight time from 30 hr up to 70 hr. In addition, an aerogel radiator with lower index of refraction, $n = 1.043$, was employed in the CK counter to extend the energy range beyond $2 \text{ GeV nucleon}^{-1}$. After a successful launch on 2000 September 1, the top part of the Kevlar pressure vessel ruptured during ascent at an altitude of roughly 10 km. The sudden pressure drop inside the gondola caused severe damage to the detector systems and marked the end of scientific flight. Problems in the recovery led to a total loss of the instrument in a catastrophic landing.

Future experiments with comparable features of ISOMAX and improved statistics are needed to impose stronger constraints on cosmic-ray propagation models.

This experiment was supported by grant NASA RTOP 353-87-02 at Goddard, by NAG5-5227 at Caltech, and by DFG Si 290/8 at the University of Siegen, Germany. We would like to thank the many engineers and technicians that made ISOMAX a success, as well as the National Scientific Balloon Facility. In particular, we thank Donald L. Richter for his invaluable, dedicated work on balloon payloads. Thanks to A. Molnar at the University of Siegen for providing the beryllium and lithium spectra.

REFERENCES

- Ahlen, S. P., et al. 2000, *ApJ*, 534, 757
 Berezhinskii, V. S. 1990, *Astrophysics of Cosmic Rays*, ed. V. L. Ginzburg (Amsterdam: North-Holland)
 Buffington, A., Orth, C. D., & Mast, T. S. 1978, *ApJ*, 226, 355
 Byrnak, B., et al. 1983, in *Proc. 18th Int. Cosmic Ray Conf. (Bangalore)*, 9, 135
 Connell, J. J. 1998, *ApJ*, 501, L59
 Davis, A., et al. 2000, *ACE CRIS Level 2 Data* (Pasadena: Caltech), http://www.srl.caltech.edu/ACE/ASC/level2/lv2DATA_CRIS.html
 de Nolfo, G. A., et al. 1999, in *Proc. 26th Int. Cosmic Ray Conf. (Salt Lake City)*, 3, 29
 ———. 2001, in *Proc. 27th Int. Cosmic Ray Conf. (Hamburg)*, 5, 1659
 ———. 2003, in *Proc. 28th Int. Cosmic Ray Conf. (Tsukuba)*, 4, 1777
 Dwyer, R. 1978, *ApJ*, 224, 691
 Engelmann, J. J., et al. 1990, *A&A*, 233, 96
 Garcia-Munoz, M., Mason, G. A., & Simpson, J. A. 1975, *ApJ*, 201, L145
 ———. 1977, in *Proc. 15th Int. Cosmic Ray Conf. (Plovdiv)*, 1, 301
 Garcia-Munoz, M., Simpson, J. A., & Wefel, J. P. 1981, in *Proc. 17th Int. Cosmic Ray Conf. (Paris)*, 2, 72
 Gibner, P. S., et al. 1992, *ApJ*, 391, L89
 Ginzburg, V. L., & Ptuskin, V. S. 1976, *Rev. Mod. Phys.*, 48, 161
 Göbel, H., et al. 2001, in *Proc. 27th Int. Cosmic Ray Conf. (Hamburg)*, 5, 1663
 Golden, R. L., et al. 1991, *Nucl. Instrum. Methods Phys. Res. A*, 306, 366
 Gupta, S. K., et al. 1997, *Nucl. Instrum. Methods Phys. Res. A*, 400, 428
 Hagen, F. A., Fisher, A. J., & Ormes, J. F. 1977, *ApJ*, 212, 262
 Hams, T., et al. 1999, in *Proc. 26th Int. Cosmic Ray Conf. (Salt Lake City)*, 3, 121
 ———. 2001, in *Proc. 27th Int. Cosmic Ray Conf. (Hamburg)*, 5, 1655
 Hof, M., et al. 1994, *Nucl. Instrum. Methods Phys. Res. A*, 345, 569
 ———. 2000, *Nucl. Instrum. Methods Phys. Res. A*, 454, 180
 Kox, S., et al. 1987, *Phys. Rev. C*, 35, 1678
 Krombel, K. E., & Wiedenbeck, M. E. 1988, *ApJ*, 328, 940
 Mewaldt, R. A., et al. 1981, *ApJ*, 251, L27
 Mitchell, J. W., et al. 1999, *Proc. 26th Int. Cosmic Ray Conf. (Salt Lake City)*, 3, 113
 Molnar, A., & Simon, M. 2003, in *Proc. 28th Int. Cosmic Ray Conf. (Tsukuba)*, 4, 1937
 Moskalenko, I. V. 2003, in *Proc. 28th Int. Cosmic Ray Conf. (Tsukuba)*, rapporteur talk (astro-ph/0405532)
 Moskalenko, I. V., & Strong, A. W. 2000, *Ap&SS*, 272, 247

- Moskalenko, I. V., et al. 2003, in Proc. 28th Int. Cosmic Ray Conf. (Tsukuba), 4, 1917
- Poelz, G., & Riethmüller, R. 1982, Nucl. Instrum. Methods Phys. Res. A, 195, 491
- Prishchep, V. L., & Ptuskin, V. S. 1975, Ap&SS, 32, 265
- Ptuskin, V. S., & Soutoul, A. 1998, A&A, 337, 859
- Raisbeck, G. M., & Yiou, F. 1971, Phys. Rev. Lett., 27, 875
- Silberberg, R., et al. 1998, ApJ, 501, 911
- Simon, M. 1999, in Topics in Cosmic-Ray Astrophysics, ed. M. DuVernois (Commack: Nova Science Publishers), 99
- Smith, B., & McDonald, F. B. 1981, in Proc. 17th Int. Cosmic Ray Conf. (Paris), 9, 138
- Soutoul, A., et al. 1983, in Proc. 18th Int. Cosmic Ray Conf. (Bangalore), 9, 143
- Stephens, S. A., & Streitmatter, R. E. 1998, ApJ, 505, 266
- Streitmatter, R. E., & Stephens, S. A. 2001, Adv. Space Res., 27, 743
- Streitmatter, R. E., et al. 1995, ISOMAX Proposal SSC-4A (Greenbelt: NASA/GSFC)
- Tsao, C. H., et al. 1998, ApJ, 501, 920
- Webber, W. R., & Kish, J. 1979, in Proc. 16th Int. Cosmic Ray Conf. (Kyoto), 1, 389
- Webber, W. R., Kish, J. C., & Schrier, D. A. 1990, Phys. Rev. C, 41, 547
- Webber, W. R., Lukasiak, A., & McDonald, F. B. 1997, ApJ, 476, 766
- . 2002, ApJ, 568, 210
- Webber, W. R., et al. 1977, Astrophys. Lett., 18, 125
- . 1998, ApJ, 508, 949
- Wiedenbeck, M. E., & Greiner, D. E. 1980, ApJ, 239, L139
- Yanasak, N. E., et al. 2001, ApJ, 563, 768